


## RESEARCH ARTICLE

# A Human-derived Dual MRI/PET Reporter Gene System with High Translational Potential for Cell Tracking

Nourhan Shalaby<sup>1</sup> , John Kelly<sup>2</sup>, Francisco Martinez<sup>2</sup>, Mathew Fox<sup>3,4</sup>, Qi Qi<sup>1</sup>, Jonathan Thiessen<sup>2,4,5</sup>, Justin Hicks<sup>2,3,5</sup>, Timothy J. Scholl<sup>1,2,6</sup>, and John A. Ronald<sup>1,2,3</sup>

<sup>1</sup>Department of Medical Biophysics, Schulich School of Medicine and Dentistry, Western University, London, Canada

<sup>2</sup>Robarts Research Institute, Schulich School of Medicine and Dentistry, Western University, London, Canada

<sup>3</sup>Lawson Health Research Institute, London, Canada

<sup>4</sup>Saint Joseph's Health Care, Toronto, Canada

<sup>5</sup>Lawson Cyclotron and Radiochemistry Facility, London, Canada

<sup>6</sup>Ontario Institute for Cancer Research, Toronto, Canada 2022

### Abstract

**Purpose:** Reporter gene imaging has been extensively used to longitudinally report on whole-body distribution and viability of transplanted engineered cells. Multi-modal cell tracking can provide complementary information on cell fate. Typical multi-modal reporter gene systems often combine clinical and preclinical modalities. A multi-modal reporter gene system for magnetic resonance imaging (MRI) and positron emission tomography (PET), two clinical modalities, would be advantageous by combining the sensitivity of PET with the high-resolution morphology and non-ionizing nature of MRI. **Procedures:** We developed and evaluated a dual MRI/PET reporter gene system composed of two human-derived reporter genes that utilize clinical reporter probes for engineered cell detection. As a proof-of-concept, breast cancer cells were engineered to co-express the human organic anion transporter polypeptide 1B3 (OATP1B3) that uptakes the clinical MRI contrast agent gadolinium ethoxybenzyl-diethylenetriaminopentaacetic acid (Gd-EOB-DTPA), and the human sodium iodide symporter (NIS) which uptakes the PET tracer, [<sup>18</sup>F] tetrafluoroborate ([<sup>18</sup>F] TFB).

**Results:** T<sub>1</sub>-weighted MRI results in mice exhibited significantly higher MRI signals in reporter-gene-engineered mammary fat pad tumors versus contralateral naïve tumors ( $p < 0.05$ ). No differences in contrast enhancement were observed at 5 h after Gd-EOB-DTPA administration using either intravenous or intraperitoneal injection. We also found significantly higher standard uptake values (SUV) in engineered tumors in comparison to the naïve tumors in [<sup>18</sup>F]TFB PET images ( $p < 0.001$ ). Intratumoral heterogeneity in signal enhancement was more conspicuous in relatively higher resolution MR images compared to PET images.

**Conclusions:** Our study demonstrates the ability to noninvasively track cells engineered with our human-derived dual MRI/PET reporter system, enabling a more comprehensive evaluation of transplanted cells. Future work is focused on applying this tool to track therapeutic cells, which may one day enable the broader application of cell tracking within the healthcare system.

**Keywords** Reporter genes · Reporter probes · Contrast agents · MRI · PET · Cell tracking

## Introduction

Reporter genes are highly advantageous tools for in vivo cell tracking in that only viable cells are detected and they allow for life-long tracking capability because they are passed on to daughter cells [1]. Reporter genes have been developed for many in vivo preclinical and clinical imaging modalities such as fluorescence imaging (FLI) [2–4], bioluminescence imaging (BLI) [5, 6], magnetic resonance imaging (MRI) [7–9], ultrasound [10, 11], photoacoustic imaging [12], single photon emission computed tomography (SPECT), and positron emission tomography (PET) [13–15]. Notably, first-in-man clinical cell tracking has been achieved using a virally derived PET reporter gene engineered into therapeutic T cells infused intracranially in glioma patients [14, 16].

A multiple modality reporter gene system would be beneficial as it would combine the strengths of each modality to hopefully mitigate individual weaknesses. Typical multi-modal reporter gene imaging systems incorporate optical imaging via fluorescence and/or bioluminescence in combination with nuclear imaging [17–23]. While FLI and BLI provide great sensitivity ( $10^{-15}$  mol/L for BLI) [24], and high throughput at a relatively lower cost, they suffer from low spatial resolution at depth, light scattering, and are not compatible for imaging larger subjects, thus limiting their potential for clinical translation. For multi-modal tracking of cellular therapeutics in patients, a human-derived reporter gene system combining two clinical modalities would be of great benefit. MRI provides excellent soft-tissue contrasts with high spatial resolution, lacks ionizing radiation, and is relatively cost-effective and readily available in the clinic, while PET can offer sensitive and quantitative information on administered cells. Here, we develop a clinically relevant dual modality reporter gene system for cellular imaging with both MRI and PET. Our main interest in combining these two modalities is that the fine spatial resolution of MRI can provide information about intratumoral heterogeneity of viable cells, while PET's sensitivity would be valuable when MRI is not sufficiently sensitive to detect smaller lesions. Moreover, combining both modalities may allow more widespread use within the healthcare system where one modality may not be as readily available (e.g., PET).

The organic anion transporter polypeptide (OATP) is a superfamily of membrane transporters that can uptake a variety of multi-specific anionic substrates, both endogenous and exogenous, from the blood and into the cells for their absorption, distribution, metabolism, and excretion [25]. Brindle et al. were the first to demonstrate specific uptake of a clinically approved  $Gd^{3+}$  MRI agent by rat-derived OATP1A1 transport, showing a rapid, reversible, and strong increase in the signal enhancement of OATP1A1-expressing cells on  $T_1$ -weighted MRI [26]. Additionally, OATP1A1 was established as a multi-modal reporter gene as it was also shown to uptake the  $^{111}In$ -EOB-DTPA analog for detection with SPECT [27], as well as the clinical agent, indocyanine green (ICG), for detection with photoacoustic imaging [12]. OATP1B3

is a human-derived transporter of the OATP1 family, with restricted background expression, mainly in the basolateral membrane of hepatocytes in the liver [25]. In addition to a wide variety of compatible substrates, OATP1B3 can uptake the MRI contrast agent Gd-EOB-DTPA, developed for liver imaging, enabling the OATP1B3 to serve as an MRI reporter gene [28–30]. Importantly, the human origin of this gene overcomes safety limitations, such as the potential immunogenicity of analogous rodent-derivatives or alternative prokaryotic-derived reporter genes.

The human sodium iodide symporter (NIS) has been previously demonstrated as a reporter gene for SPECT or PET detection [31–34]. This symporter is naturally expressed on the basolateral surface of follicular cells of the thyroid and functions to uptake plasma iodide for either oxidation or entrapment and storage for eventual catabolism into thyroid hormones [35]. Lower expression levels of NIS have also been reported in the salivary glands, stomach, and lactating mammary glands with no ability for entrapment and hormone production [36]. Additionally, a wide selection of tracers has been developed for diagnostic or therapeutic purposes involving NIS-expressing tissue [37–39]. [ $^{18}F$ ]tetrafluoroborate ([ $^{18}F$ ]TFB) has been extensively evaluated as a PET reporter probe for imaging NIS expression in both transfected [34, 40] and transduced cells [41]. In comparison to other NIS compatible probes, [ $^{18}F$ ]TFB is an ideal PET tracer as it is a fundamental NIS substrate without any other metabolic interactions [42]. Furthermore, Fluorine-18 tracers have a high positron yield of 97%, with a short diffusion range in tissue (<2.4 mm), a clinically compatible half-life of 110 min, and may be routinely synthesized in medical centers with cyclotrons [39].

In this research, we have designed, developed, and evaluated a dual MRI/PET human reporter gene system for in vivo cellular imaging. This system uses two human-derived reporter genes (NIS and OATP1B3), with their respective clinical imaging probes ([ $^{18}F$ ]TFB and Gd-EOB-DTPA, respectively) to enable detection with two clinical imaging technologies, giving this system high translational potential.

## Materials and Methods

### *Cell Lines and Cell Cultures*

Human triple-negative breast cancer cells (MDA-MB-231) obtained from American Type Culture Collection (Manassas, Virginia, United States) were maintained in Dulbecco's modified Eagle's medium (DMEM) containing 10% fetal bovine serum (Wisent BioProducts, Quebec, Canada), 1% penicillin, and 1% streptomycin (Waltham, Thermo Fisher Scientific Inc., Massachusetts, United States). All cells were kept in a humidified incubator with 5%  $CO_2$  at 37 °C. Cells were routinely confirmed to be mycoplasma negative using the MycoAlert mycoplasma detection kit (Lonza Group, Basel, Switzerland).

## Cloning and Lentiviral Production

A third-generation lentiviral transfer plasmid was engineered to express the NIS gene (Origene Technologies, Inc. NM\_000453), OATP1B3 (sequence acquired from the hOATP1B3/SLCO1B3 VersaClone cDNA vector, Cat. RDC0870, R&D Systems, Minneapolis, Minnesota, United States), along with the zsGreen (zsG) fluorescence reporter gene, driven by a constitutive hEF1 $\alpha$  promoter. NIS, OATP1B3, and zsG are separated with the self-cleaving peptides T2A and P2A, respectively. P2A and T2A are reported to have the highest (> 90%) cleaving efficiencies among other 2As [43, 44], warranting equimolar expression of each reporter gene (Fig. 1A). Third-generation packaging and envelop plasmids pMDLg/pRRE, pRSV-Rev, and pMD2.G (Addgene plasmids #12,251, #12,253, and #12,259, respectively) were combined with the transfer plasmid for the In-Fusion Cloning reaction (Takara Bio USA, Inc.) to transfect human embryonic kidney (HEK 293 T) (American Type Culture collection; ATCC) cells with the aid of Lipofectamine 3000 (Thermo Fisher Scientific, Massachusetts, USA) in accordance to the manufacturer's lentiviral production protocol (Thermo Fisher Scientific Inc., Waltham, Massachusetts, United States). Viral-containing supernatant was collected 24 h and 48 h after transfection, filtered with a 0.45  $\mu$ m filter and frozen at  $-80^{\circ}\text{C}$  until use.

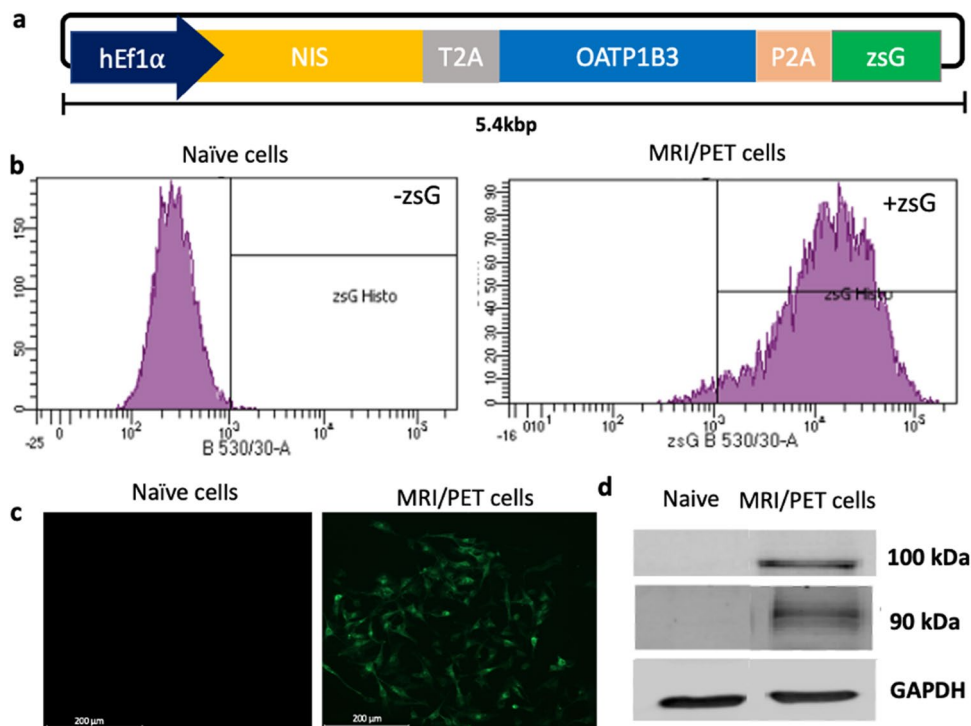
## Cell Transduction

MDA-MB-231 cells were seeded at a density of  $5 \times 10^5$  cells per well in a 6-well plate on day 0 and then transduced for 6 h on day 1 with the prepared lentivirus and Polybrene (8  $\mu$ g/ml; Sigma) at a multiplicity of infection (MOI) of one. On day 4, naïve and transduced cells were harvested and assessed for zsG expression and sorted using a FACSAria III fluorescence-activated cell sorter (BD Biosciences) to acquire a highly purified population of engineered cells, which we call our MRI/PET cells throughout. Fluorescence microscopy was performed on an LSM Meta 510 microscope (Carl Zeiss AG, Oberkochen, Germany) to confirm the presence of zsG in the MRI/PET cells.

## Western Blots

Western blot analysis for both OATP1B3 and NIS was performed using naïve MDA-MB-231 cells, MDA-MB-231 cells expressing OATP1B3 alone and our MRI/PET cells. Cells were incubated with 200- $\mu$ L  $4^{\circ}\text{C}$  RIPA buffer and protease inhibitors for 30 min. Lysates were collected and sonicated with three 5.0-s, 40-kHz bursts before centrifugation at 13,000G for 20 min at  $4^{\circ}\text{C}$ . Supernatants were collected and quantified using the Pierce BCA Protein Assay (23,225, Thermo Fisher Scientific, Massachusetts, USA). A 40- $\mu$ g protein sample was loaded into an acrylamide gel composed of a 4.0% stacking layer buffered at pH 6.8 and a 15% separation layer buffered at pH 8.8. Gel electrophoresis was performed for 20 min at 90 V and 1 h at 110 V. Protein

**Fig. 1** (A) Diagram of hEF1 $\alpha$ -hNIS-T2A-OATP1B3-P2A-zsG lentiviral construct used to engineer MDA-MB-231 triple-negative cells. (B) Flow cytometry showing naïve cells with no zsG expression and transduced MRI/PET cells with 93% transduction efficiency post-sort. (C) Fluorescence microscopy images showing no zsG in naïve cells and MRI/PET cells showing zsG fluorescence signal. (D) Western blots of naïve and transduced cells showing the NIS and OATP1B3 bands at their corresponding sizes (100 kDa and 90 kDa, respectively) and their absence in the naïve cells



was transferred to a nitrocellulose membrane for 7.5 min via the iBlot™ 2 Gel Transfer Device (IB21001, Thermo Fisher Scientific, Waltham, Massachusetts, United States) and blocked with 0.05% Tween-20, 3% w/v BSA solution for 30 min. For OATP1B3, a primary purified rabbit antibody against OATP1B3 (1:500 dilution, ab139120, Abcam, Cambridge, United Kingdom) was added for overnight incubation at 4 °C. For the myc-tagged NIS, a mouse anti-myc (9B11, Cell Signaling Technology, Massachusetts, USA) was added at a dilution of 1:1000 for 1 h at room temperature. After washing the blot three times with 0.05% Tween-20 solution for 5 min, the OATP1B3 secondary antibody, Goat anti-Rabbit IgG (H + L) Highly Cross-Adsorbed Secondary Antibody, Alexa Fluor 790, was used with a dilution of 1:10,000 (A11369, Thermo Fisher Scientific, Massachusetts, USA) was added for 1 h. The blot was washed three times with 0.05% Tween-20 solution for 5 min before application of the Goat anti-Mouse IgG (H + L) High Cross-Adsorbed Secondary Antibody, Alexa Fluor Plus 488, with a dilution of 0.1–0.4 µg/ml (A32723, Thermo Fisher Scientific, Massachusetts, USA) for 1 h. Lastly, the blot was stripped for GAPDH staining. A primary mouse anti-GAPDH antibody (MAB374, Sigma-Aldrich, Missouri, USA) at a dilution of 1:1000 was applied for 1 h at room temperature with subsequent application of secondary antibodies IRDye-800CW and 680RD (Thermo Fisher Scientific, Massachusetts, USA) at dilutions of 1:15,000. Finally, imaging on the Odyssey CLx Imaging System (LI-COR Biosciences, Lincoln, Nebraska, United States) was performed.

### *In Vitro* Gd-EOB-DTPA Uptake and MRI

One million naïve or MRI/PET cells/ml were seeded in two 15-cm-diameter dishes. At 95% cell confluency, a 1.6-mM dose of Gd-EOB-DTPA (Eovist/Primovist®, Bayer Health Care Pharma, Berlin, Germany) was added to each dish and incubated for 60 min. Each cell type also had a dish with no Gd-EOB-DTPA addition to serve as the negative control. Media was aspirated, and cells were thoroughly washed with 1 × phosphate-buffered saline (PBS) (pH 7.4) three times. Subsequent trypsinization, collection, and centrifugation of cells formed cell pellets in 0.2 ml Eppendorf tubes. Tubes were imbedded into a 1% agarose gel phantom for MRI imaging with a 3 T GE clinical MR scanner (General Electric Healthcare Discovery MR750 3.0 T, Milwaukee, Wisconsin, United States) using a 16-channel head RF coil. A fast spin-echo inversion-recovery pulse sequence, with the below parameters (Table 1), was used to determine spin–lattice relaxation rates by sampling with the following 17 inversion times (TI): 50 ms, 60 ms, 68 ms, 80 ms, 94 ms, 128 ms, 175 ms, 239 ms, 327 ms, 447 ms, 612 ms, 836 ms, 1144 ms, 1564 ms, 2139 ms, 2925 ms, and 4000 ms. MatLab (R2018a, MathWorks, Natick, Massachusetts, United States) was used to evaluate spin–lattice relaxation rates by overlaying the image series of the different inversion times and computing the average signal intensity for each cell pellet. The data were

**Table 1** MRI sequence parameters used for *in vitro* uptake of Gd-EOB-DTPA. (Inversion times are listed in the text.)

Imaging matrix size	256 × 256
Repetition time (TR)	5000 ms
Echo time (TE)	19.1 ms
Echo train length (ETL)	4
Number of averages (NEX)	1
Receiver bandwidth	24.4 kHz
In-plane resolution	0.27 mm × 0.27 mm
Slice thickness	2.0 mm

fitted with Eq. (1) to determine the spin–lattice relaxation time ( $T_1$ ).

$$s = M_0 \left( 1 - 2e^{-\frac{TI}{T_1}} + e^{-\frac{TR}{T_1}} \right) \quad (1)$$

Here,  $S$  represents the acquired signal intensity,  $M_0$  is the magnetization in steady state,  $TI$  is the inversion time, and  $TR$  is the repetition time.

### *In Vitro* [<sup>18</sup>F]TFB Tracer Uptake

[<sup>18</sup>F]TFB was synthesized as described previously [41] with 98.7 ± 2% purity. [<sup>18</sup>F]TFB uptake studies were performed with naïve and MRI/PET cells. Cells were seeded in a 6-well dish (5 × 10<sup>5</sup> cells/well) and incubated (37 °C with 5% CO<sub>2</sub>) overnight. DMEM was aspirated, and cells were washed with 1 × PBS. Fresh DMEM was added (2 ml/well), followed by the addition of 0.1 MBq of [<sup>18</sup>F]TFB to each well. Cells were incubated for 30 min prior to their collection. The activity of harvested cells as well as the activity in the supernatant were measured using a gamma counter. Counts were decay-corrected, and tracer uptake was calculated as the average counts per minute (cpm) of activity detected using the following equation.

$$\text{Uptake}(\%) = \frac{CPM_{\text{cells}}}{(CPM_{\text{cells}} + CPM_{\text{supernatant}})} \times 100\% \quad (2)$$

### *Animal Model*

All applicable institutional and/or national guidelines for the care and use of animals were followed. Naïve and MRI/PET MDA-MB-231 cells were implanted into the left and right mammary fat pad, respectively, of female NOD scid gamma (NSG) mice ( $n = 3$ ). Tumors were allowed to form for ~2–3 weeks, and imaging was performed on day 19 with PET, 31 and 35 with MRI post-implantation.

### *In Vivo* Gd-EOB-DTPA-enhanced MRI

$T_1$ -weighted 3 T-MRI was performed pre and 4.5 h post-tail-vein injection of 1 mmol/kg Gd-EOB-DTPA. To evaluate

signal resulting from agent uptake and retention, one mouse implanted with separate naïve and engineered tumors was serially imaged for approximately 5 h after Gd-EOB-DTPA intravenous and intraperitoneal injections on separate days. Gd-EOB-DTPA was administered by IV tail injections on day 31 post-tumor implantation and by IP injections on day 35 post-tumor implantation in 3 NSG mice to assess different delivery methods. All mice were anesthetized with 1–2% isoflurane during imaging sessions with the use of a nose cone attached to a carbon charcoal filter for passive scavenging. Mice respiration rates during acquisition were between 40 and 70 bpm, and body temperature was maintained between 37 °C and 38 °C using a regulated heating pad. A 3D Spoiled Gradient Recalled Acquisition in Steady State (SPRG) pulse sequence with a 3.5-cm-diameter birdcage RF coil (Morris Instruments, Ottawa, ON, Canada) and a custom-built gradient insert were used with the below parameters (Table 2) for a scan time of approximately 15 min. Horos Project software v3.3.6 (horosproject.org, Nimble Co LLC d/b/a Purview, Annapolis, Maryland, United States) was used to manually segment regions-of-interest (ROIs) to acquire measures of signal intensity on pre-contrast and post-contrast images in naïve, MRI/PET tumors as well as other organs (muscle, kidney, liver, and bladder).

### *In Vivo* [<sup>18</sup>F]TFB PET

Nineteen days post-cell implantation, mice were anesthetized with 2% isoflurane, injected with 13–15 MBq of [<sup>18</sup>F]TFB in 50–150 μL, and imaged dynamically with a microPET system (Siemens Inveon ©2011 by Siemens Medical Solutions USA, Inc.). Animal breathing rate and body temperature were monitored and maintained between 40 and 70 bpm and at 37 °C, respectively. Dynamic PET data were acquired for 40 min, and images were reconstructed using 2D filtered back projection. Quantification of PET signal was performed by manual segmentation of ROIs using Horos Project software v3.3.6. Maximum activity projections (MAPs) were generated. SUV was calculated with the below equation:

$$SUV\left(\frac{g}{mL}\right) = \frac{Pixelvalue\left(\frac{Bq}{mL}\right) * weight(kg)}{Dose(Bq)} * 1000\left(\frac{g}{kg}\right) \quad (3)$$

**Table 2** MRI sequence parameters used for in vivo mice imaging

Imaging matrix size	250 × 250
Repetition time (TR)	14.7 ms
Echo time (TE)	3.3 ms
Number of averages (NEX)	3
Flip angle	60°
Field of view (FOV)	50 mm
Bandwidth	24.4 kHz
In-plane resolution	0.2 mm × 0.2 mm
Slice thickness	0.2 mm

### *Histology and Immunofluorescence Staining*

Supplementary Fig. 1 shows the H&E staining of both naïve and MRI/PET cells on the left panels. Cells were grown on a coverslip, fixed in 4% PFA, permeabilized with Triton X-100 for 10 min, and incubated for 1 h at room temperature with rabbit anti-SLCO1B3 (OATP1B3) primary antibody (2-μg/ml working concentration, HPA004943, Sigma-Aldrich Canada, Oakville, Ontario, Canada). Secondary Goat anti-rabbit AlexaFluor 647-conjugated secondary antibody was then applied for 1 h (1:500 dilution; 4-μg/ml working concentration, ab150079, Lot E114795, Abcam, Cambridge, Massachusetts, United States). Mouse anti-NIS primary antibody was used at a dilution of 1:100 (113,168, SLC5A5 Polyclonal Antibody, Thermo Fisher Scientific Inc., Massachusetts, United States) for 2 h at room temperature. Coverslips were washed three times with PBS, and secondary antibody Goat anti-rabbit at a dilution of 1:200 (Alexa Fluor® 488, Thermo Fisher Scientific Inc., Massachusetts, United States) was used for 1 h. Cells were counterstained with DAPI for 5 min and imaged with the LSM Meta 510 microscope (Carl Zeiss AG, Oberkochen, Germany).

### *Statistics*

Unpaired two-tailed *t*-tests were performed using Graphpad Prism software (Version 7.00 for Mac OS X, GraphPad Software Inc., La Jolla California USA, [www.graphpad.com](http://www.graphpad.com)) for cell characterization after Gd-EOB-DTPA and [<sup>18</sup>F]TFB incubation and comparing MRI data between IP and IV at 5 h. Repeated measures of ANOVA were used for SUV comparisons. All data are expressed as mean ± standard deviation of at least three independent experiments. *P*-values < 0.05 were considered statistically significant.

## Results

Human breast cancer cells were engineered to stably co-express NIS, OATP1B3, and zsG using a lentivirus produced using the transfer plasmid shown in Fig. 1A. Flow cytometry showed no zsG expression in naïve cells and a 93% transduction efficiency in the dual reporter gene system containing zsG (Fig. 1B). Fluorescence microscopy confirmed zsG positive cells in the MRI/PET cells and no zsG in naïve cells (Fig. 1C). Western blots confirmed the presence of both transporters in the MRI/PET cells with a band at 100 kDa corresponding to NIS and a 90-kDa band for the OATP1B3 protein (Fig. 1D). These bands were not observed for the naïve cells.

Next, we evaluated reporter gene functionality in vitro. MRI/PET cells incubated with Gd-EOB-DTPA resulted in a 38% higher *R<sub>f</sub>* value compared to naïve cells incubated with Gd-EOB-DTPA (*p* < 0.05). The average *R<sub>f</sub>* for naïve cells was 0.76 ± 0.08 Hz, compared to 1.05 ± 0.12 Hz for MRI/PET cells (Fig. 2B). Similarly, cells were also incubated with 0.1 MBq of [<sup>18</sup>F]TFB for 1 h, and the percentage activity

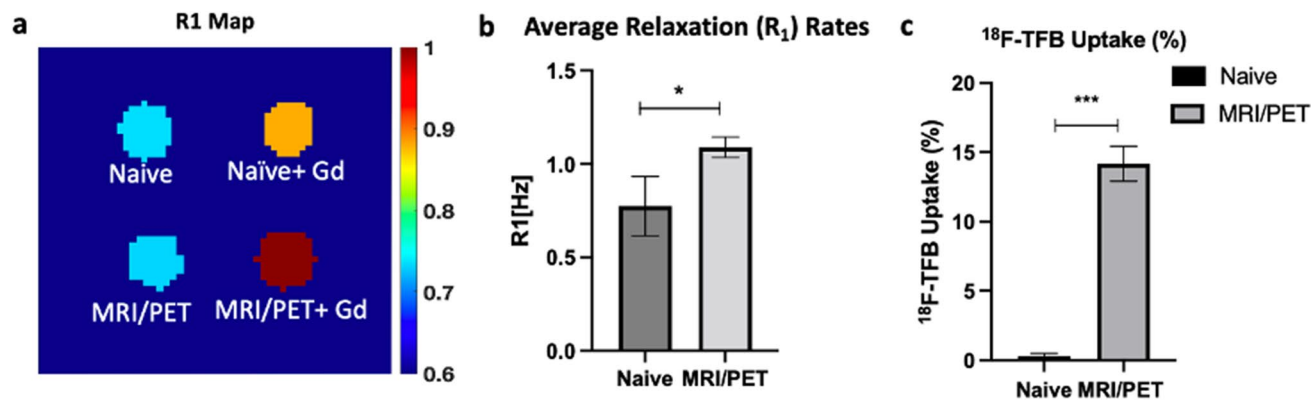


**Fig. 2** (A) An average  $R_1$  map in naïve and MRI/PET cells without and with incubation of Gd-EOB-DTPA. (B)  $R_1$  values (38% higher) in MRI/PET cells incubated with the Gd-EOB-DTPA were found significantly higher ( $p < 0.05$ ) compared to the naïve cells incubated with the agent. (C) [ $^{18}\text{F}$ ]TFB percent uptake was calculated as  $0.31 \pm 0.18\%$  in naïve cells, whereas significantly higher uptake was seen in MRI/PET cells ( $14.2 \pm 1.3\%$ ;  $*p < 0.001$ )

uptake was retrieved with a gamma counter. NIS-OATP1B3 cells incubated with [ $^{18}\text{F}$ ]TFB had an uptake of  $14.2 \pm 1.3\%$  compared to  $0.31 \pm 0.18\%$  uptake of naïve cells, revealing a 45-fold higher ( $p < 0.001$ ) uptake in the dual reporter gene cells, as shown in Fig. 2C. Additionally, functionality test results for Gd-EOB-DTPA uptake in Naïve, NIS/zsG, OATP1B3/zsG, and NIS/OATP1B3/zsG cells, showing non-significant uptake between OATP1B3/zsG and NIS/OATP1B3/zsG cells, are shown in Supplementary Fig. 2.

### *In vivo* Gd-EOB-DTPA-enhanced OATP1B3 MRI

#### Intravenous (IV) versus Intraperitoneal (IP) Gd-EOB-DTPA Administration

Typical OATP1/Gd-EOB-DTPA reporter gene imaging is performed ~4–6 h post-IV administration [27]. Several studies have compared contrast enhancement in MRI using both an IP and IV method of agent administration and have shown IP as an alternative delivery route that yields comparable contrast enhancement to IV [45, 46]. The dynamics of the MRI/PET cells to accumulate Gd-EOB-DTPA in vivo through IV or IP administration was investigated 30 days post-tumor implantation in one mouse. This longitudinal study was only performed on one mouse as per our institution requirements; Fig. 3A shows dynamic coronal images over the course of ~4.5 h with both naïve (left) and MRI/PET (right) tumors post-IV administration of the Gd-EOB-DTPA with a dose of 1 mmol/kg. As expected, no differences in signal were apparent between the tumors in the pre-contrast image. Post-contrast images showed obvious contrast enhancement only in the MRI/PET tumor, with enhancement being heterogeneous within the tumor (Fig. 3C). Image analysis revealed higher signal intensity in the dual MRI/PET compared to naïve tumor (Fig. 3B) within 1-h post-injection of Gd-EOB-DTPA with relatively

constant uptake for the remaining of the imaging period. Contrast enhancement was also observed in the liver, presumably through uptake by endogenous murine OATP1A1 expression (Supplementary Fig. 3).

The same mouse in Fig. 3 was dynamically imaged again at 34 days post-tumor implantation for about 5.5 h using the same MR imaging parameters but with IP delivery of Gd-EOB-DTPA (1 mmol/kg). It should be noted that due to the mean clearance half-life of Gd-EOB-DTPA (55–57 min), <1% of the agent amount is expected to remain 24 h post-administration; Fig. 4A shows select MRI images pre- and post-Gd-EOB-DTPA administration with IP injection. At around 1.5 h, contrast enhancement surrounding both naïve and MRI/PET mammary fat pad tumors is present. Over time, more agent accumulates intratumorally in the MRI/PET tumor compared to the naïve tumor, corresponding to higher  $T_1$ -weighted signal intensities (Fig. 5B). Again, heterogeneous enhancement within the MRI/PET tumors was noted. Contrast enhancement in the liver with natural OATP1 expression was also observed (Supplementary Fig. 3). Supplementary Fig. 5 shows the difference in signal intensity between MRI/PET and naïve tumors in our dynamic imaging for both IV and IP injection, showing the highest difference after approximately 2.5 h for IV and 5 h for IP injection.

Figure 5 shows pre- and approximately 5 h post-Gd-EOB-DTPA injection with both IV (top) and IP (bottom) delivery routes. (Supplementary Fig. 4 shows representative examples at selective time points.) Differences in signal enhancement are evident between the naïve and the MRI/PET tumor approximately 5 h post-agent administration with both delivery methods. Significantly higher ( $p < 0.05$ ) average signal intensity was observed in MRI/PET tumors compared to naïve tumors in all three mice for both IV and IP administration of Gd-EOB-DTPA (B). No differences in signal intensity were seen between IV or IP injection route at this time point post-Gd-EOB-DTPA injection.

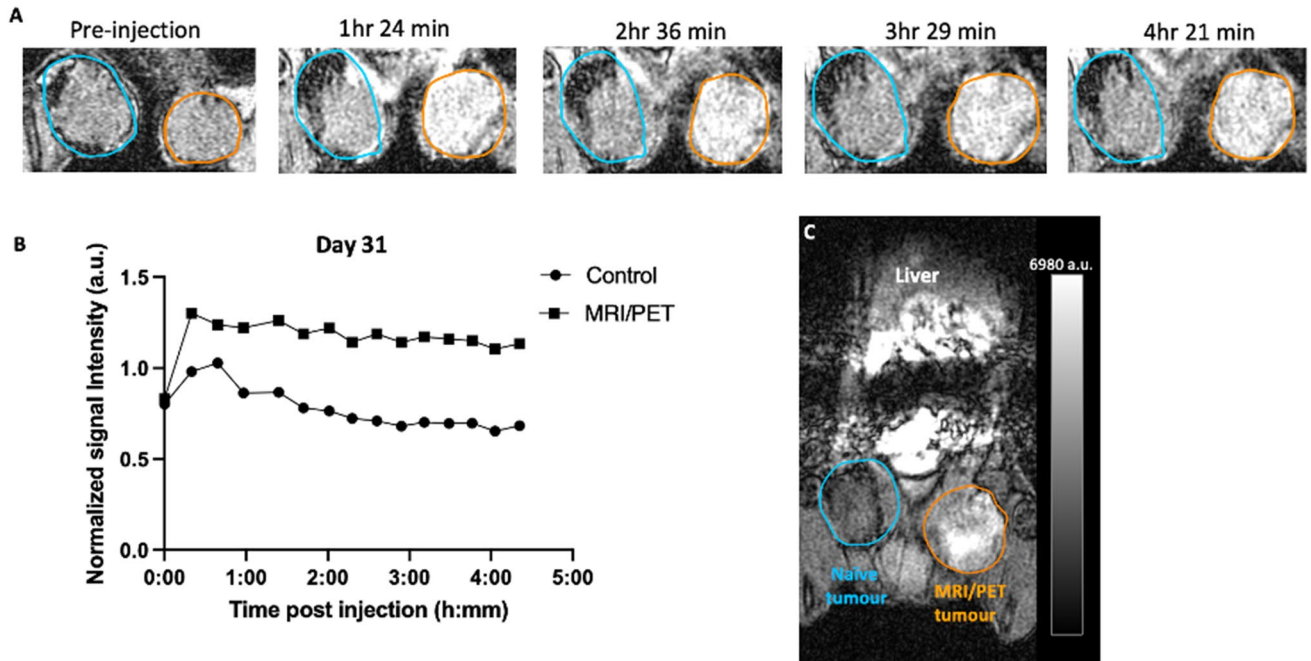


**Fig. 3** (A) Dynamic coronal  $T1$ -w MRI images of lower mammary fat pads of an NSG mouse after IV Gd-EOB-DTPA injection. Manual segmentation showing naïve (left; blue outline) and MRI/PET (right; orange outline) tumors pre- and post-IV administration of Gd-EOB-DTPA. (B) Enhanced contrast and higher normalized (to muscle tissue) signal intensities are shown in the MRI/PET tumor. (C) Contrast enhancement was also observed in endogenous tissue and clearance into the intestines

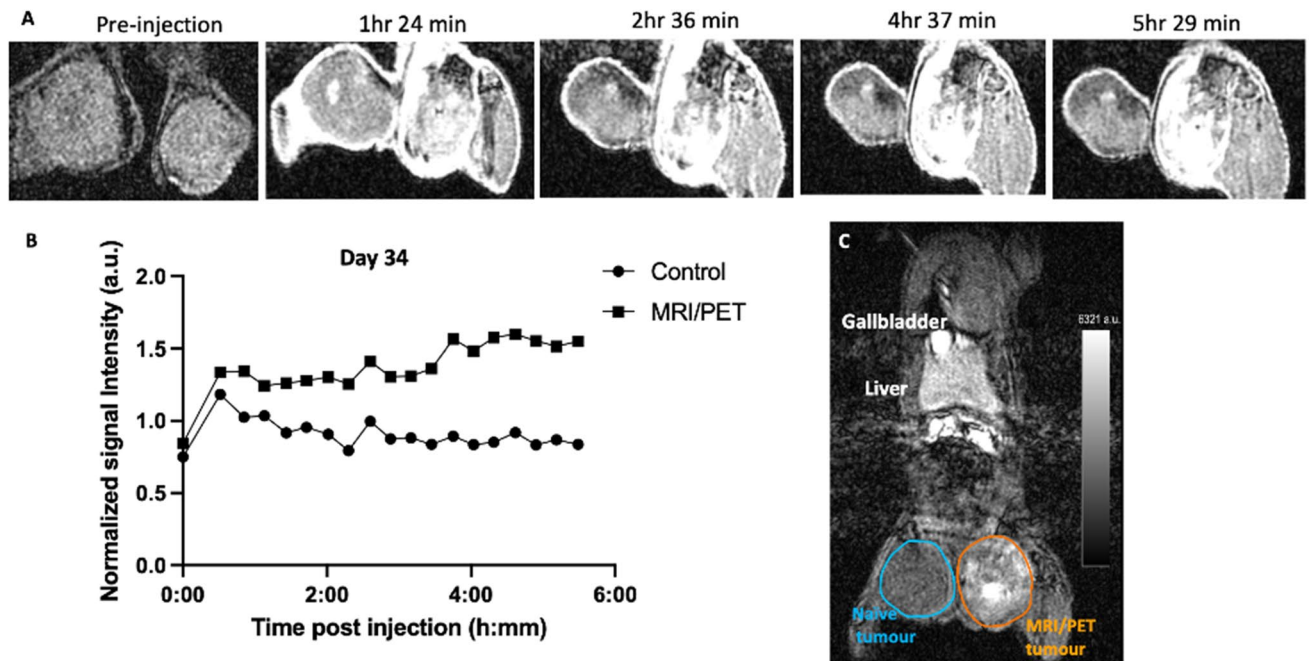


**Fig. 4** (A) Dynamic coronal  $T1$ -w MRI images of lower mammary fat pads of an NSG mouse after IP Gd-EOB-DTPA injection. Manual segmentation showing naïve (left) and NIS-OATP1B3 (right) tumors pre- and post-IP administration of Gd-EOB-DTPA. (B) Higher normalized (to muscle tissue) signal intensities are shown in the NIS-OATP1B3 tumor compared to the naïve tumor. (C) Contrast enhancement was also observed in the liver

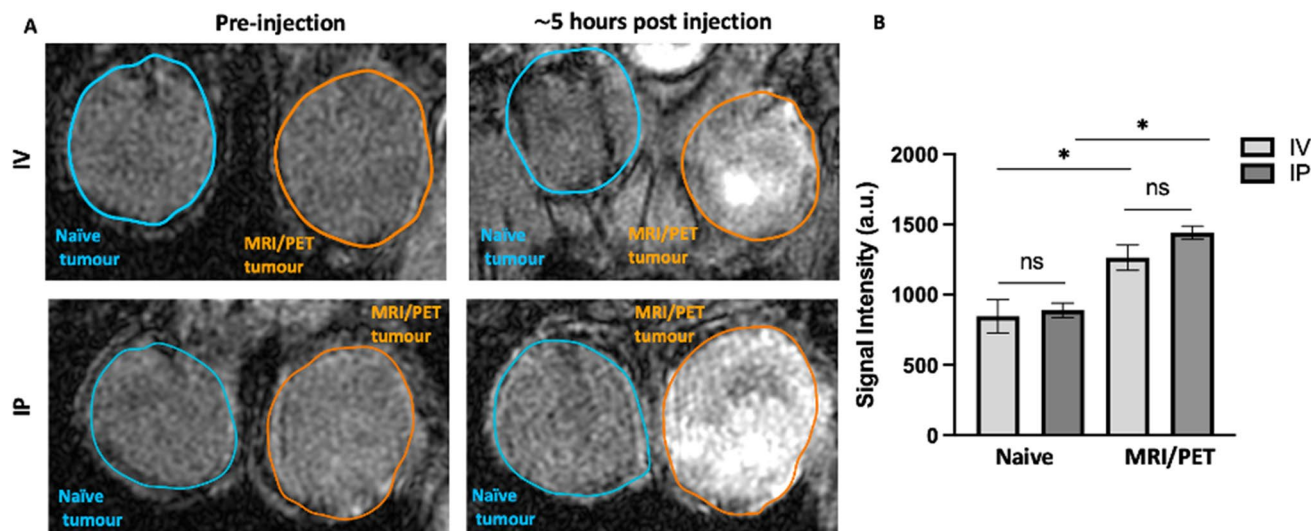


**Fig. 5** (A) Representative  $T_1$ -weighted MRI images showing pre- and approximately 5 h post-IV (top) and IP (bottom) injection of Gd-EOB-DTPA in two different mice. (B) Contrast enhancement observed in MRI/PET tumors post-Gd-EOB-DTPA injection, with both IV and IP administration methods. No contrast enhancement was observed in the naïve tumors post-agent administration. Significantly higher average signal intensity between MRI/PET tumors and naïve tumors was observed for both IV and IP agent administration, and no significant difference in average signal intensity between IV and IP delivery methods was observed for either naïve or MRI/PET tumors ( $n=3$ ) at 5 h post-injection

### In vivo [ $^{18}\text{F}$ ]TFB NIS PET

Mice bearing contralateral naïve and MRI/PET mammary fat pad tumors received 13–15 MBq of [ $^{18}\text{F}$ ]TFB via tail vein injection, and dynamic PET imaging was performed for 40 min (Fig. 6). Rapid accumulation of [ $^{18}\text{F}$ ]TFB in NIS-expressing tissue was observed within 10 min of injection (Fig. 6A, B). As expected, whole-body PET mean activity projections (MAPs) displayed regions of [ $^{18}\text{F}$ ]TFB uptake in the salivary glands, thyroid, and stomach which correspond to sites of endogenous mouse NIS expression. SUV values in the thyroid and stomach over time are shown in Supplementary Fig. 6. Tracer uptake was also observed in the engineered MRI/PET tumor, but not in the naïve tumor (Fig. 6A, C). Qualitatively, unlike with our MRI results, local differences in tracer uptake in different regions within tumors were difficult to visualize in our PET images due to the image resolution. The average SUV was calculated for mice at different time points during the 40-min scan (Fig. 3B). Significantly higher SUVs were observed for MRI/PET tumor compared to naïve tumors 10 min, 15 min, 20 min, 25 min, 30 min, 35 min, and 40 min after tracer injection ( $p<0.05$ ). Supplementary Fig. 7 shows the effect size, calculated as the difference in SUV between MRI/PET and naïve tumors divided by the uncertainty in their difference, showing the maximum effect size at 30 min.

## Discussion

The use of multiple modalities is advantageous as it harnesses complementary information from individual modalities to provide a more comprehensive assessment of the activity

and fate of administered cells. Sensitive imaging modalities often suffer from relatively lower resolution (BLI, PET, SPECT), whereas less sensitive modalities may provide fine spatial resolution (MRI) [24]. As a result, multi-modal tracking is often undertaken with a combination of sensitive and spatially resolving modalities [47]. However, current multi-modal cell tracking methods possess limitations either in their safety profiles [14, 48], their imaging sensitivity [49–51], their preclinical status [19, 52], or their ability for long-term tracking [53, 54], limiting their translational potential.

For this work, we combine two clinical systems to exploit the sensitivity and quantification of PET and the higher spatial resolution and soft-tissue contrast of MRI. We have developed a novel multi-modal cell tracking system using MRI and PET human-derived reporter genes that can provide safe, sensitive, and quantitative information for longitudinal tracking.

We employed the human-derived OATP1B3 gene as an MRI reporter gene for our system. This transporter can transport the clinical Gd-EOB-DTPA MRI contrast agent into cells. Once internalized, the Gd-EOB-DTPA enhances contrast on  $T_1$ -weighted images to improve the conspicuity of engineered cells. Previous work by Brindle's group showed maximal contrast enhancement in  $T_1$ -weighted images 5 h post-IV injection of Gd-EOB-DTPA in OATP1A1-expressing cells [27]. In this work, we performed dynamic imaging to determine the optimal timing of the maximum contrast uptake within our OATP1B3-engineered tumors.

We also compared the contrast enhancement of the Gd-EOB-DTPA agent via two administration routes: intravenously (IV) and intraperitoneally (IP). Although probes are typically administered intravenously, IP administration



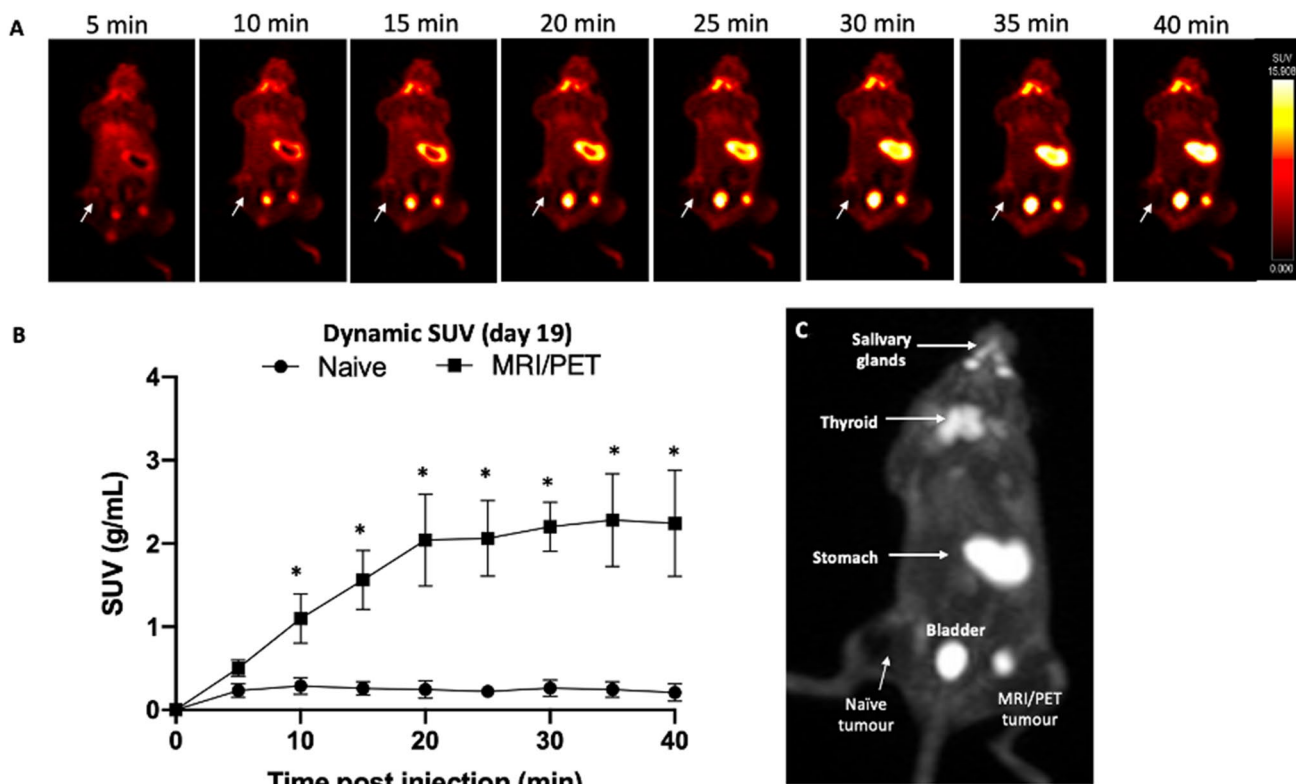


**Fig. 6** (A) Dynamic MAPs showing whole-body PET coronal images and uptake of [ $^{18}\text{F}$ ]TFB for 40 min. (B) Average SUV (g/ml) for 3 mice at different time points showed significantly higher for MRI/PET tumors compared to naïve tumors ( $p < 0.05$ ) using repeated measures of ANOVA. (C) Displaying [ $^{18}\text{F}$ ]TFB uptake in NIS-expressing tissue (salivary glands, thyroid, stomach), MRI/PET tumor (denoted with arrowhead), and the bladder ( $^{18}\text{F}$ ]TFB clearance)

is a technically easier injection that has shown comparable contrast enhancement and can be used as a substitute to IV injections in small animal models for targeting and trapping agents [45, 46]. However, IP pharmacokinetics dictate that the contrast material would be absorbed into the peritoneal cavity and eventually drain into the portal vein for hepatic metabolism before reaching systemic circulation, resulting in a slower delivery of the agent when compared to IV injection routes. Maximum contrast enhancement was achieved approximately 2 h post both IV and IP injection routes, and significant enhancement was endured for the remaining of the imaging period (~5 h). Thus, the OATP1B3 gene demonstrated genuine potential for cell tracking in gadolinium-enhanced MRI with both IV and IP delivery methods of the Gd-EOB-DTPA contrast agent.

NIS was employed as the PET reporter gene for this system, and its expression was imaged with PET following administration of its clinical tracer, [ $^{18}\text{F}$ ]TFB. Our dual MRI/PET reporter system also showed significant uptake of [ $^{18}\text{F}$ ]TFB ( $p < 0.001$ ) in vitro and higher ( $p < 0.05$ ) in vivo SUV in the NIS-expressing tumors compared to the naïve tumors.

An additional qualitative difference between the PET and MRI images is the ability to distinguish intratumoral heterogeneity of signal enhancement. While PET is more sensitive, we were only able to see heterogeneous contrast enhancement

in the OATP1B3-expressing tumors in the MRI images. Previous work from our lab has shown this variation in contrast enhancement corresponds to the spatial distribution of viable OATP1A1-expressing cells [9].

Advances in cellular therapies have demonstrated anti-tumor effects by modifying a variety of cell types to boost their targeting and killing abilities [55]. In vivo tracking of these therapeutic cells can reveal information regarding their cellular interactions, therapeutic efficacy, as well as potential side effects [47]. In addition to assessing the number of therapeutic cells within tumors, it is also important to evaluate their tumor localization and distribution. Thus, combining the quantitative nature of PET and the fine resolution of MRI can produce information on both the cell numbers and their location, respectively.

Ideally, for safety concerns, reporter genes should be human-derived genes as opposed to exogenous reporter genes (luciferase or fluorescent protein) which can trigger an immune response. Indeed the virally derived PET reporter gene herpes simplex virus thymidine kinase has been shown to be immunogenic in man [56], highlighting a need to reduce immunogenicity via protein engineering or utilizing human-derived reporter genes. NIS and OATP1B3 are both endogenous human genes, making them non-immunogenic to facilitate clinical translation. Furthermore, both imaging

probes ( $[^{18}\text{F}]\text{TfB}$  and Gd-EOB-DTPA) are already widely in clinical use with PET and MRI, respectively, further giving this system high translational potential. Repeated administration of these imaging probes allows for longitudinal tracking to be accomplished in reporter gene systems for a specific application. Administration of  $[^{18}\text{F}]\text{TfB}$  for detection of NIS expression with PET can provide sensitive and quantifiable information and detection at an earlier timepoint but may be limited by cost, availability, and perceived concerns regarding radiation. In contrast, Gd-EOB-DTPA can be repetitively administered to facilitate the longitudinal tracking of engineered cells with MRI. Moreover, the fine spatial resolution of MRI images can show intratumoral heterogeneity of the viable engineered cells. Heterogeneity due to differences in biodistribution within the control tumor is most likely seen during the early phases after Gd-EOB-DTPA administration when non-specific uptake into the extracellular space is dominant. At earlier time points, there is non-specific uptake in both control and MRI/PET tumors (following both IV and IP injections). Over time, there is no significant Gd-EOB-DTPA enhancement in control tumors, and uptake is specific to OATP1B3-expressing cells.

This study validates a new dual PET and MRI reporter gene system for in vivo cell tracking. Future incorporation of this dual reporter gene system in other cell types, such as T lymphocytes, natural killer (NK) cells, mesenchymal stem cells, or dendritic cells, could provide valuable information for more clinically relevant applications. Additionally, novel gene integration systems such as CRISPR/Cas with the ability to target safe genomic sites could further improve the safety of this cell tracking multi-modal reporter gene system while reducing the chances of unwanted biological effects on the cells [57].

## Conclusion

In this work, MRI and PET were used to detect cells longitudinally. To our knowledge, this is the first time this combination of clinical imaging modalities has been used with reporter gene imaging. We demonstrated that we could use a multi-modal imaging system to visualize human-derived MRI/PET reporter gene-expressing cells, enabling a more comprehensive understanding of administered cells. Future applications of such systems can be used for tracking therapeutic cells.

*Supplementary Information* The online version contains supplementary material available at <https://doi.org/10.1007/s11307-021-01697-8>.

*Acknowledgements* This study was funded by the Ontario Institute for Cancer Research (IA-028) National Institutes of Health (1UH2EB028907-01), Translational Breast Cancer Research Unit, and the National Science and Engineering Research Council of Canada.

*Author Contribution* All authors contributed to the conception or design of the work or the acquisition, analysis, or interpretation of data for the work. All authors contributed to drafting the work or revising it critically

for important intellectual content. All authors approved the final version of the manuscript to be published. All authors agree to be accountable for all aspects of the work in ensuring that questions related to the accuracy or integrity of any part of the work are appropriately investigated and resolved.

## Declarations

**Conflict of Interest** The authors declare that they have no conflict of interest.

## References

- Ashmore-Harris C, Iafrate M, Saleem A, Fruhwirth GO (2020) Non-invasive reporter gene imaging of cell therapies, including T cells and stem cells. *Mol Ther* 28. <https://doi.org/10.1016/j.ymthe.2020.03.016>
- Yang Z, Wang Y, Li Y et al (2014) Options for tracking GFP-Labeled transplanted myoblasts using in vivo fluorescence imaging: implications for tracking stem cell fate. *BMC Biotechnol* 14:1–8. <https://doi.org/10.1186/1472-6750-14-55>
- Xu X, Yang Z, Liu Q, Wang Y (2010) In vivo fluorescence imaging of muscle cell regeneration by transplanted EGFP-labeled myoblasts. *Mol Ther* 18:835–842. <https://doi.org/10.1038/mt.2010.3>
- Winnard PT, Kluth JB, Raman V (2006) Noninvasive optical tracking of red fluorescent protein-expressing cancer cells in a model of metastatic breast cancer. *Neoplasia* 8:796–806. <https://doi.org/10.1593/neo.06304>
- Conway M, Xu T, Kirkpatrick A et al (2020) Real-time tracking of stem cell viability, proliferation, and differentiation with autonomous bioluminescence imaging. *BMC Biol* 18:79. <https://doi.org/10.1186/s12915-020-00815-2>
- Parkins KM, Dubois VP, Kelly JJ et al (2020) Engineering circulating tumor cells as novel cancer theranostics. *Theranostics* 10:7925–7937. <https://doi.org/10.7150/thno.44259>
- Bar-Shir A, Alon L, Korner MJ et al (2018) Quantification and tracking of genetically engineered dendritic cells for studying immunotherapy. *Magn Reson Med* 79:1010–1019. <https://doi.org/10.1002/mrm.26708>
- Kim HS, Woo J, Lee JH et al (2015) In vivo tracking of dendritic cell using MRI reporter gene. *Ferritin PLoS One* 10:e0125291. <https://doi.org/10.1371/journal.pone.0125291>
- Nyström NN, Hamilton AM, Xia W et al (2019) Longitudinal visualization of viable cancer cell intratumoral distribution in mouse models using Oatp1a1-enhanced magnetic resonance imaging. *Invest Radiol* 54:302–311. <https://doi.org/10.1097/RLI.0000000000000542>
- Bourdeau RW, Lee-Gosselin A, Lakshmanan A et al (2018) Acoustic reporter genes for noninvasive imaging of microorganisms in mammalian hosts. *Nature* 553:86–90. <https://doi.org/10.1038/nature25021>
- Farhadi A, Ho GH, Sawyer DP, et al (2019) Ultrasound imaging of gene expression in mammalian cells. *Science* 365(80):1469–1475. <https://doi.org/10.1126/science.aax4804>
- Nyström NN, Yip LCM, Carson JJJ et al (2019) Development of a human photoacoustic imaging reporter gene using the clinical dye indocyanine green. *Radiol Imaging Cancer* 1:e190035. <https://doi.org/10.1148/rycan.2019190035>
- Yaghoubi SS, Campbell DO, Radu CG, Czernin J (2012) Positron emission tomography reporter genes and reporter probes: gene and cell therapy applications. *Theranostics* 2:374–391
- Keu KV, Witney TH, Yaghoubi S, et al (2017) Reporter gene imaging of targeted T cell immunotherapy in recurrent glioma. *Sci Transl Med* 9. <https://doi.org/10.1126/scitranslmed.aag2196>
- Gschweng EH, McCracken MN, Kaufman ML et al (2014) HSV-sr39TK positron emission tomography and suicide gene elimination of human hematopoietic stem cells and their progeny in humanized mice. *Cancer Res* 74:5173–5183. <https://doi.org/10.1158/0008-5472.CAN-14-0376>
- Yaghoubi SS, Jensen MC, Satyamurthy N et al (2009) Noninvasive detection of therapeutic cytolytic T cells with  $^{18}\text{F}$ -FHBG PET in a patient with glioma. *Nat Clin Pract Oncol* 6:53–58. <https://doi.org/10.1038/ncponc1278>
- Pomper MG, Hammond H, Yu X et al (2009) (2008) Serial imaging of human embryonic stem-cell engraftment and teratoma formation in live mouse models. *Cell Res* 19(3):370–379. <https://doi.org/10.1038/cr.2008.329>

18. Y W, WY Z, S H, et al (2012) Genome editing of human embryonic stem cells and induced pluripotent stem cells with zinc finger nucleases for cellular imaging. *Circ Res* 111:1494–1503. <https://doi.org/10.1161/CIRCRESAHA.112.274969>
19. Z L, F W, J D, et al (2007) Imaging of mesenchymal stem cell transplant by bioluminescence and PET. *J Nucl Med* 48:2011–2020. <https://doi.org/10.2967/JNUMED.107.043166>
20. E W, B H, L O, et al (2017) Molecular imaging of human embryonic stem cells stably expressing human PET reporter genes after zinc finger nuclease-mediated genome editing. *J Nucl Med* 58:1659–1665. <https://doi.org/10.2967/JNUMED.117.189779>
21. H T, X L, H G, et al (2012) Radio-deoxynucleoside analogs used for imaging tk expression in a transgenic mouse model of induced hepatocellular carcinoma. *Theranostics* 2:597–606. <https://doi.org/10.7150/THNO.3371>
22. Lin KM, Hsu C-H, Chang W-SW, et al (2008) Human breast tumor cells express multimodal imaging reporter genes. *Mol Imaging Biol* 2008 105 10:253–263. <https://doi.org/10.1007/S11307-008-0147-2>
23. Yan X, Ray P, Paulmurugan R et al (2013) A transgenic tri-modality reporter mouse. *PLoS ONE* 8:e73580. <https://doi.org/10.1371/JOURNAL.PONE.0073580>
24. Xing Y, Zhao J, Conti PS, Chen K (2014) Radiolabeled nanoparticles for multimodality tumor imaging. *Theranostics* 4:290–306
25. Zhou Y, Yuan J, Li Z et al (2015) Genetic polymorphisms and function of the organic anion-transporting polypeptide 1A2 and its clinical relevance in drug disposition. *Pharmacology* 95:201–208. <https://doi.org/10.1159/000381313>
26. Jacquemin E, Hagenbuch B, Stieger B et al (1994) Dual-modality gene reporter for in vivo imaging. *Proc Natl Acad Sci U S A* 91:133–137. <https://doi.org/10.1073/pnas.91.1.133>
27. Jacquemin E, Hagenbuch B, Stieger B et al (2014) Expression cloning of a rat liver Na(+)-independent organic anion transporter. *PNAS* 91:133–137. <https://doi.org/10.1073/pnas.91.1.133>
28. Leonhardt M, Keiser M, Oswald S et al (2010) Hepatic uptake of the magnetic resonance imaging contrast agent Gd-EOB-DTPA: role of human organic anion transporters. *Drug Metab Dispos* 38:1024–1028. <https://doi.org/10.1124/dmd.110.032862>
29. Wu M-R, Liu H-M, Lu C-W et al (2018) Organic anion-transporting polypeptide 1B3 as a dual reporter gene for fluorescence and magnetic resonance imaging. *FASEB J* 32:1705–1715. <https://doi.org/10.1096/fj.201700767R>
30. Baek SE, Ul-Haq A, Kim DH et al (2020) Human organic anion transporting polypeptide 1B3 applied as an MRI-based reporter gene. *Korean J Radiol* 21:726–735. <https://doi.org/10.3348/kjr.2019.0903>
31. Sharif-Paghaleh E, Sunassee K, Tavaré R, et al (2011) In vivo SPECT reporter gene imaging of regulatory T cells. *PLoS One* 6. <https://doi.org/10.1371/journal.pone.0025857>
32. Punzón I, Mauduit D, Holvoet B et al (2020) In vivo myoblasts tracking using the sodium iodide symporter gene expression in dogs. *Mol Ther - Methods Clin Dev* 17:317–327. <https://doi.org/10.1016/j.omtm.2019.12.011>
33. Volpe A, Man F, Lim L, et al (2018) Radionuclide-fluorescence reporter gene imaging to track tumor progression in rodent tumor models. *J Vis Exp*. <https://doi.org/10.3791/57088>
34. Lee SB, Lee HW, Lee H, et al (2017) Tracking dendritic cell migration into lymph nodes by using a novel PET probe 18F-tetrafluoroborate for sodium/iodide symporter. *EJNMMI Res* 7. <https://doi.org/10.1186/s13550-017-0280-5>
35. Ahn BC (2012) Sodium iodide symporter for nuclear molecular imaging and gene therapy: from bedside to bench and back. *Theranostics* 2:392–402
36. Penheiter AR, Russell SJ, Carlson SK (2012) The sodium iodide symporter (NIS) as an imaging reporter for gene, viral, and cell-based therapies. *Curr Gene Ther* 12:33. <https://doi.org/10.2174/156652312799789235>
37. Willhauck MJ, Sharif Samani B-R, Gildehaus F-J et al (2007) Application of 188Rhenium as an alternative radionuclide for treatment of prostate cancer after tumor-specific sodium iodide symporter gene expression. *J Clin Endocrinol Metab* 92:4451–4458. <https://doi.org/10.1210/jc.2007-0402>
38. Smit JWA, Schröder-Van Der Elst JP, Karperien M et al (2002) Iodide kinetics and experimental 131I therapy in a xenotransplanted human sodium-iodide symporter-transfected human follicular thyroid carcinoma cell line. *J Clin Endocrinol Metab* 87:1247–1253. <https://doi.org/10.1210/jcem.87.3.8307>
39. Jiang H, DeGrado TR (2018) [18F]Tetrafluoroborate ([18F]TFB) and its analogs for PET imaging of the sodium/iodide symporter. *Theranostics* 8:3918–3931. <https://doi.org/10.7150/tno.24997>
40. Weeks AJ, Jauregui-Osoro M, Cleij M et al (2011) Evaluation of [18F]-tetrafluoroborate as a potential PET imaging agent for the human sodium/iodide symporter in a new colon carcinoma cell line, HCT116, expressing hNIS. *Nucl Med Commun* 32:98–105. <https://doi.org/10.1097/MNM.0b013e3283419540>
41. Jiang H, Bansal A, Pandey MK et al (2016) Synthesis of 18F-Tetrafluoroborate via radiofluorination of boron trifluoride and evaluation in a murine C6-Glioma tumor model. *J Nucl Med* 57:1454–1459. <https://doi.org/10.2967/jnumed.115.170894>
42. Diocou S, Volpe A, Jauregui-Osoro M et al (2017) [18F]tetrafluoroborate-PET/CT enables sensitive tumor and metastasis in vivo imaging in a sodium iodide symporter-expressing tumor model. *Sci Rep* 7:946. <https://doi.org/10.1038/s41598-017-01044-4>
43. Liu Z, Chen O, Wall JBJ et al (2017) Systematic comparison of 2A peptides for cloning multi-genes in a polycistronic vector. *Sci Rep* 7:2193. <https://doi.org/10.1038/s41598-017-02460-2>
44. Wang Y, Wang F, Wang R et al (2015) 2A self-cleaving peptide-based multi-gene expression system in the silkworm *Bombyx mori*. *Sci Rep* 5:16273. <https://doi.org/10.1038/srep16273>
45. Jing Ye, Liu X, Xu Y, Lü G (2006) Targeted magnetic resonance imaging with intraperitoneal and intravenous streptavidin (SA)-DTPA-Gd: a comparative study in tumor-bearing nude mice. <https://pubmed.ncbi.nlm.nih.gov/16503514/>. Accessed 15 dec 2020
46. Moreno H, Hua F, Brown T, Small S (2006) Longitudinal mapping of mouse cerebral blood volume with MRI. *NMR Biomed* 19:535–543. <https://doi.org/10.1002/mbm.1022>
47. Perrin J, Capitaio M, Mougin-Degraef M et al (2020) Cell Tracking in Cancer Immunotherapy. *Front Med* 7:34
48. C B, ME F, EH W, SR R (2006) Analysis of transgene-specific immune responses that limit the in vivo persistence of adoptively transferred HSV-TK-modified donor T cells after allogeneic hematopoietic cell transplantation. *Blood* 107:2294–2302. <https://doi.org/10.1182/BLOOD-2005-08-3503>
49. Fruhwirth GO, Diocou S, Blower PJ et al (2014) A whole-body dual-modality radionuclide optical strategy for preclinical imaging of metastasis and heterogeneous treatment response in different microenvironments. *J Nucl Med* 55:686–694. <https://doi.org/10.2967/jnumed.113.127480>
50. Stammes MA, Knol-Blankevoort VT, Cruz LJ et al (2016) (2016) Pre-clinical evaluation of a cyanine-based SPECT probe for multimodal tumor necrosis imaging. *Mol Imaging Biol* 186(18):905–915. <https://doi.org/10.1007/S11307-016-0972-7>
51. Stammes MA, Maeda A, Bu J, et al (2016) The necrosis-avid small molecule HQ4-DTPA as a multimodal imaging agent for monitoring radiation therapy-induced tumor cell death. *Front Oncol* 0:221. <https://doi.org/10.3389/FONC.2016.00221>
52. Pool SE, Hagen TLM ten, Koelewijn S, et al (2012) Multimodality imaging of somatostatin receptor-positive tumors with nuclear and bioluminescence imaging: 11:27–32. <https://doi.org/10.2310/7290.2011.00024>
53. Bhattacharya A, Kochhar R, Sharma S et al (2014) PET/CT with 18F-FDG-labeled autologous leukocytes for the diagnosis of infected fluid collections in acute pancreatitis. *J Nucl Med* 55:1267–1272. <https://doi.org/10.2967/JNUMED.114.137232>
54. Hofmann M, Wollert KC, Meyer GP et al (2005) Monitoring of bone marrow cell homing into the infarcted human myocardium. *Circulation* 111:2198–2202. <https://doi.org/10.1161/01.CIR.0000163546.27639.AA>
55. Guedan S, Ruella M, June CH (2018) Emerging cellular therapies for cancer. 101146/ANNUREV-IMMUNOL-042718-041407 37:145–171. <https://doi.org/10.1146/ANNUREV-IMMUNOL-042718-041407>
56. R G, G O, MT S, et al (2015) Improving the safety of cell therapy with the TK-suicide gene. *Front Pharmacol* 6. <https://doi.org/10.3389/FPHAR.2015.00095>
57. Dubois VP, Zotova D, Parkins KM et al (2018) Safe harbor targeted CRISPR-Cas9 tools for molecular-genetic imaging of cells in living subjects. *Cris J* 1:440–449. <https://doi.org/10.1089/crispr.2018.0030>